International Journal of Nanomedicine

Dovepress
Taylor & Francis Group

Open Access Full Text Article

ORIGINAL RESEARCH

Boosting Hydroxyl Radical Generation with Nitrogen Vacancy–Modified Carbon Nitride for Triggering Dual Damage of Cancer Nucleus DNA–Mitochondria against Hypoxic Tumors

Yuan Zhang[1,2,*], Meixian Liu[1,2,*], Shuyun Xue[1,2], Na Li[1,2], Jinjia Hong[1,2], Jiawen Gu[1,2], Xiaoyan Ren[1,2], Huifei Li[1,2], Jie Xu[1,2], Chengxi Zhang[1,2], Tianqi Liang[1,2], Bin Zhao[1,2], Xing Wang[1,2]

[1]Department of Oral and Maxillofacial Surgery, Shanxi Medical University School and Hospital of Stomatology, Taiyuan, 030001, People's Republic of China; [2]Shanxi Province Key Laboratory of Oral Diseases Prevention and New Materials, Taiyuan, 030001, People's Republic of China

*These authors contributed equally to this work

Correspondence: Xing Wang, Shanxi Medical University School and Hospital of Stomatology, Xinjian South Road 63#, Taiyuan, 030001, People's Republic of China, Email kqwx100@163.com; Bin Zhao, Email sxmu0688@126.com

International Journal of Nanomedicine downloaded from https://www.dovepress.com/
For personal use only.

Introduction: Oral squamous cell carcinoma (OSCC) is a prevalent and deadly cancer, with over 350,000 new cases yearly. A hypoxic tumor microenvironment is the bottleneck of photodynamic therapy (PDT) and significantly weakens overall therapeutic efficacy.

Methods: In this study, we introduce nitrogen vacancy–modified PCN (N_V-PCN), a novel metal-free and O_2-independent photosensitizer designed for PDT. N_V-PCN targets Cal-27–induced OSCC by reducing highly expressed H_2O_2 in tumors to highly reactive •OH. This innovative approach aims to overcome the limitations posed by the hypoxic environment and enhance the effectiveness of PDT in treating OSCC.

Results: The introduction of N_V not only further improves the cell accessibility of PCN by increasing the content of $-NH_2$ but also provides more reactive sites for H_2O_2 reduction and facilitates carrier separation. Under illumination, N_V-PCN generates a burst of •OH around the nuclei and mitochondria of Cal-27 cells, which effectively kills the cells via synchronously leading to DNA damage and mitochondrial dysfunction. Compared to the conventional photosensitizer chlorin e6, N_V-PCN–based PDT exhibits excellent anticancer performance in vitro and in vivo, highlighting its potential as a next-generation therapeutic agent.

Conclusion: Collectively, the high •OH-generation efficiency, strong anticancer activity, and overall safety of the O_2-independent nanoparticle opens up new avenues for in-depth study on carbon nitride-based cancer PDT strategies. This work offers new hope for the effective treatment of OSCC and other challenging cancers.

Keywords: photodynamic therapy, nitrogen vacancy, polymeric carbon nitride, DNA-damage repair, hydroxyl radical

Introduction

Oral squamous cell carcinoma (OSCC) is a major global health issue, with over 350,000 new diagnosed cases and a high mortality rate each year.[1] Conventional surgical treatment based on removing primary lesions causes serious side effects, such as loss of facial function (chewing, swallowing, and speaking) and different levels of aesthetic change.[2] In addition, the much higher levels of DNA-damage repair in cancer cells than in normal cells can easily cause tumor resistance during radiotherapy and chemotherapy.[3]

Photodynamic therapy (PDT), with its advantages of light-controlled selectivity, minimal invasiveness, and low side effects, has garnered significant attention.[4] FDA-approved photosensitizers, such as chlorin e6 (Ce6) and 5-aminolevulinic acid, have been used to treat superficial tumors.[5,6] However, almost all solid cancers are characterized by hypoxia,

Received: 4 January 2025
Accepted: 18 June 2025
Published: 5 July 2025

© 2025 Zhang et al. This work is published and licensed by Dove Medical Press Limited. The full terms of this license are available at https://www.dovepress.com/terms.php and incorporate the Creative Commons Attribution – Non Commercial (unported, v4.0) License (http://creativecommons.org/licenses/by-nc/4.0/). By accessing the work you hereby accept the Terms. Non-commercial uses of the work are permitted without any further permission from Dove Medical Press Limited, provided the work is properly attributed. For permission for commercial use of this work, please see paragraphs 4.2 and 5 of our Terms (https://www.dovepress.com/terms.php).

and the hypoxic tumor microenvironment can reduce effectiveness of the two abovementioned agents.[7] Other photosensitizers, such as MnO_2 and Fe-MOF, can catalyze the production of highly toxic •OH with H_2O_2,[8,9] inducing multiorganelle damage in tumors. While these can be modified for targeted •OH generation, the potential release of metal ions poses a threat to health.[10,11] In the ongoing search for anticancer photocatalysts that can inflict oxygen-independent tumor damage, inhibit DNA-damage repair, and prevent organ damage from metal residues, researchers have set their sights on polymeric carbon nitride (PCN), a nanomaterial composed exclusively of carbon and nitrogen elements. Unfortunately, the PDT anticancer effect of pristine PCN is not satisfactory due to the limited •OH caused by surface inertness and severe carrier recombination.[12]

In this study, nitrogen vacancy–modified PCN (N_V-PCN) was synthesized to improve the cell accessibility of carbon nitride by increasing the content of $–NH_2$ and provide more reactive sites for H_2O_2 reduction. As presented in Figure 1, N_V-PCN leads to a synchronous explosion of •OH around the nuclei and mitochondria of Cal-27 cells under illumination, which synchronously leads to nucleus DNA damage (increased expression of double-strand break marker γH_2AX) and mitochondrial dysfunction (decreased mitochondrial membrane potential [MMP]). Mitochondrial dysfunction triggers an ROS storm to intensify DNA damage, and the ATP energy chain is attenuated to inhibit DNA-damage repair (reduced expression of 53BP1 and GADD45A). Compared to Ce6, N_V-PCN exhibits excellent anticancer performance in vitro and in vivo, opening up new avenues for carbon nitride-based cancer PDT.

Results and Discussion

Material Characterization of N_V-PCN

The morphologies of pristine PCN and N_V-PCN were observed by TEM. N_V-PCN exhibited an irregular flaked structure with a diameter of approximately 100 nm (Figure 2a), half that of PCN (Figure S1). XRD and FTIR tests were conducted to reveal the crystal phase and surface functional groups. In Figure 2b, the pristine PCN exhibits two typical diffraction peaks at 13.0° and 27.4°, which are assigned to the periodic stacking of tri-*s*-triazine rings in plane (100) and graphitic

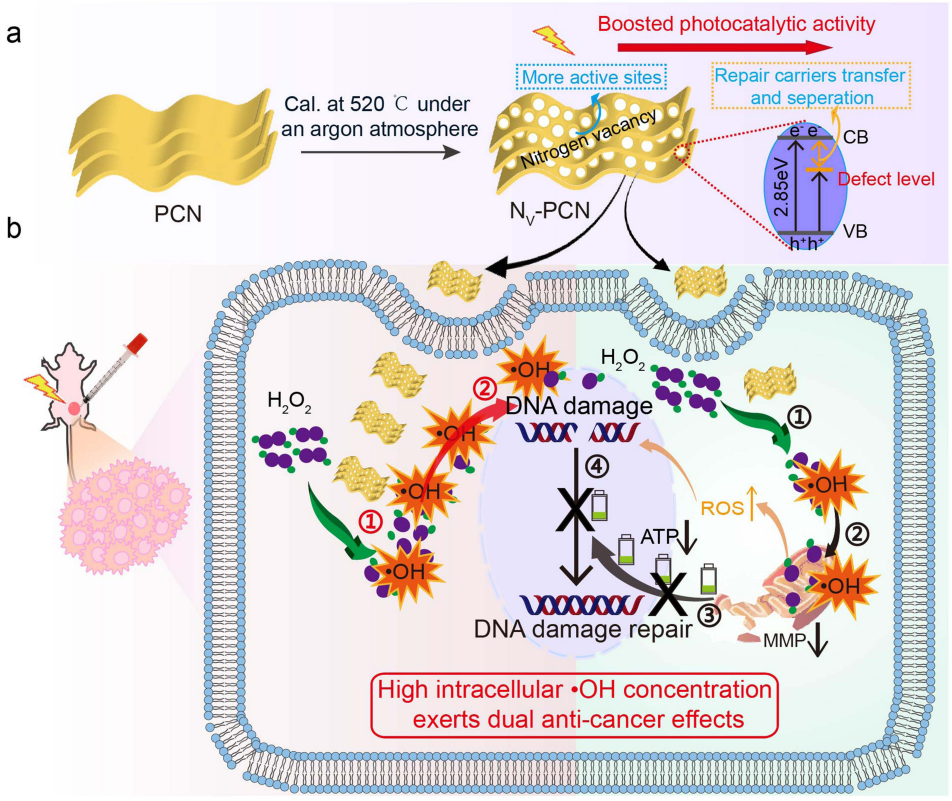

Figure 1 Schematic illustration of (**a**) the preparation process and (**b**) the therapeutic process of N_V-PCN.

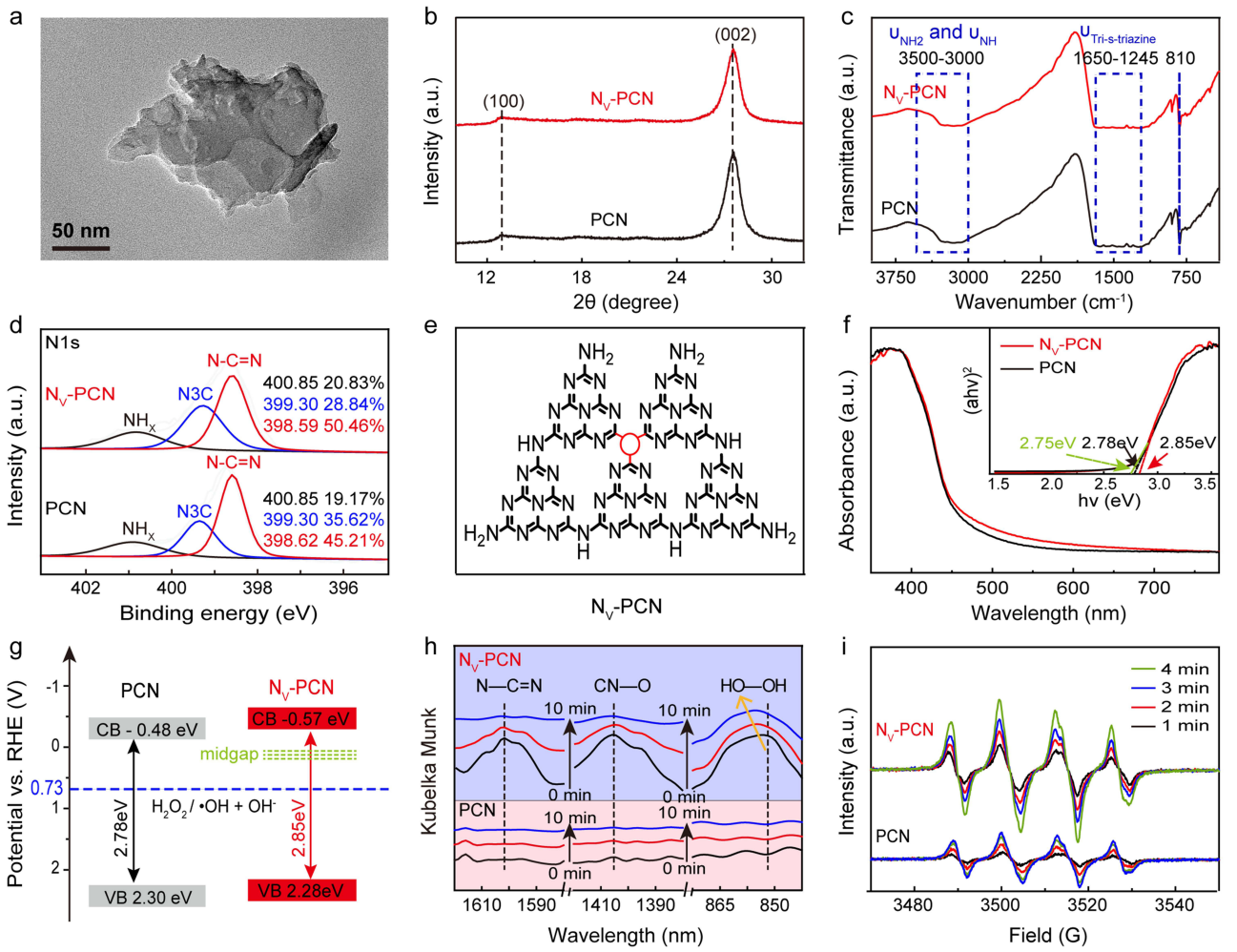

Figure 2 Characterization of as-prepared N_V-PCN. (**a**) TEM image of N_V-PCN. (**b**) XRD patterns, (**c**) FTIR spectra, and (**d**) N1s XPS signals of PCN and N_V-PCN. (**e**) Structure diagram of N_V-PCN. (**f**) UV-vis diffuse reflectance spectra. Inset: Tauc plots. (**g**) Band structures of PCN and N_V-PCN. **h**) In situ DRIFT spectra of H_2O_2 on PCN and N_V-PCN under illumination for 10 min at 5-min intervals. (**i**) In situ EPR signals of H_2O_2 over PCN and N_V-PCN under illumination.

layer (002), respectively.[13] The XRD pattern of N_V-PCN exclusively presents the diffraction peaks of the PCN component, revealing that the crystal structure of N_V-PCN is similar to that of PCN. However, all peaks of N_V-PCN weaken compared to PCN, suggesting a distorted structure and smaller dimensions of unit cells of N_V-PCN than PCN.[14] As shown in Figure 2c, PCN and N_V-PCN possess similar FTIR spectra. Specifically, the peaks at 3500–3000, 1650–1245, and 810 cm^{-1}, are attributable to the stretching vibrations of N–H group, stretching modes of tri-*s*-triazine rings in plane, and the out-of-plane bending mode of heptazine rings, respectively.[15] This indicates that the basic structure of carbon nitride was preserved during the secondary roasting process.

XPS was used to detect the type and position of vacancies formed in the secondary roasting process. As shown in Table S1, N_V-PCN (71.66%) had higher C/N (at.%) than PCN (71%), which proved that nitrogen vacancies (N_V) were introduced in carbon nitride after secondary roasting. For PCN, the three characteristic peaks at 288.30, 285.90, and 284.72 eV in C_{1s} XPS spectra (Figure S2) are attributable to N–C=N, C–NHx, and C=C (hybridized carbon in heptazine ring), respectively. The three characteristic peaks at 398.62, 399.30, and 400.85 eV in N_{1s} XPS spectra of PCN (Figure 2d) are attributable to N–C=N, N3C, and NH_X, respectively.[16] The corresponding characteristic C_{1s} and N_{1s} N–C=N peaks of N_V-PCN are shifted to lower binding energies compared with those of PCN, which can be attributed to the negative electron enrichment around N_V. To verify the position of the N vacancy in N_V-PCN, the relative content of different N species was analyzed, with results shown in Figure 2d. The peak-area ratio of N3C decreased from 35.62% in

https://doi.org/10.2147/IJN.S515726

PCN to 28.84% in N_V-PCN, which indicates that N3C defects were introduced in N_V-PCN. As shown in Figure S3, N3C has two different positions: site ① and site ②. The out-of-plane heptazine bending modes in PCN and N_V-PCN remain unchanged (Figure 2c), which excludes the generation of N3C defects at site ①. Based on these results, the structure of N_V-PCN catalyst was deduced (Figure 2e).

Since N_V-PCN was used as a PDT agent for cancer therapy, its optical properties and band structure were examined by UV-vis diffuse reflectance spectra, Tauc plots, and Mott–Schottky plots. As shown in the inset in Figure 2f, the bandgap (E_g) of PCN is 2.78 eV, which caused by the n–π* electronic transitions of the conjugated PCN framework and is close to that reported for graphitic carbon nitride.[17] Compared with PCN, N_V-PCN shows larger E_g of 2.85 eV, which is attributable to the quantum confinement effect induced by the smaller nanosheet of N_V-PCN than PCN.[18] The slightly stronger light-absorption capacity for visible light of N_V-PCN than PCN (Figure 2f) might attributable to the midgap state introduced by N_V.[19] In addition, a Mott–Schottky plot was used to obtain the semiconductor type and flat-band position of the PCN and N_V-PCN samples. As illustrated in Figure S4, the slopes of the linear parts in the two curves are positive, indicating the typical n-type semiconductor characteristics of PCN and N_V-PCN.[20] The flat-band potentials (E_{fb}) of PCN and N_V-PCN were determined to be −1.07 and −1.16 eV (vs Ag/AgCl at pH 6.6), corresponding to the conduction-band potential at −0.48 and −0.57 eV (vs RHE) (relevant equations: E(NHE) = E(Ag/AgCl) + 0.197, E(RHE) = E(NHE) + 0.0591 × pH).[21] Then, the valence-band position was calculated by adding the conduction-band potential to the bandgap, which was 2.30 eV (PCN) and 2.28 eV (N_V-PCN). Based on these results, the band structures of PCN and N_V-PCN were deduced, and these are shown in Figure 2g. Therefore, PCN and N_V-PCN have suitable band structures to catalyze the reaction of H_2O_2/•OH+ OH^-.

In situ DRIFT spectroscopy measurements (conducted in a confined space and purged for 10 min after adding H_2O_2) were performed to reveal the mechanism of photocatalytic •OH generation over PCN and N_V-PCN. As shown in Figure 2h, compared with the pristine PCN, the peak intensity is significantly enhanced after introducing N_V, indicating that N_V facilitates the adsorption of H_2O_2 on carbon nitride. The peaks at 1602, 1405, and 854 cm^{-1} can correspond to the stretching vibrations of the N–C=N bond of N_V-PCN, CN–O bond between N_V-PCN and H_2O_2, and HO–OH bonds of H_2O_2, respectively.[22] For N_V-PCN, all peaks become weaker as light-irradiation time increases and the HO–OH stretching vibration peak moves to the direction of the high wave from 850 to 856 cm^{-1}, which is attributable to the reduction in H_2O_2 by photoelectrons on N_V-PCN into •OH and OH^-. Therefore, we speculate that H_2O_2 is adsorbed on the N site of the heptazine ring attached to N_V on N_V-PCN.

To evaluate the ability of PCN and N_V-PCN to generate •OH, we examined the in situ EPR spectrum to measure •OH. Figure 2i exhibits the characteristic 1:2:2:1 •OH radical signal at different time points,[23] indicating that both PCN and N_V-PCN catalysts can reduce H_2O_2 to •OH. For PCN, •OH increases within 1–3 min, but stabilizes at 4 min, which means that the production of •OH equals annihilation.[24] For N_V-PCN, •OH continues to rise within 1–4 min, and the overall signal intensity on N_V-PCN is much more prominent than that on PCN, indicating the stronger ability of of N_V-PCN to produce •OH than PCN with equivalent PCN (×1) and even higher than threefold PCN (×3) at 4 min (Figure S5), which is attributable to the more active sites for reduction of H_2O_2 on N_V-PCN than that on PCN.

N_V-PCN Upregulated •OH Expression in Cal-27 Cells under LED Irradiation

PDT is an innovative approach in cancer treatment, offering distinct advantages over conventional therapeutic methods, such as low toxicity, precision, spatiotemporal control, and minimal invasiveness.[25] To circumvent the resistance to O_2-dependent PDT in hypoxic tumors, we designed a novel non-O_2-dependent type I photosensitizer—N_V-PCN. It is well established that the level of H_2O_2 in cancer cells is significantly higher than that in normal cells.[26] The aim of this research was to utilize N_V-PCN to convert the overexpressed H_2O_2 within tumors into highly toxic •OH, thereby destroying cancer cells. Although the generation of •OH has been investigated in material characterization, further investigation is warranted to explore its potential in biological applications.

Therefore, to further validate N_V-PCN–promoted tumoral •OH expression by PDT, Cal-27 cells were cocultured with N_V-PCN and intracellular •OH levels determined using an •OH probe, which can react with •OH generated from the reduction of H_2O_2 to emit green fluorescence. In Figure 3a, the intracellular •OH was detected via flow-cytometry analysis and CLSM imaging, respectively. As shown in Figure 3b, the ratio of •OH-producing cells is significantly

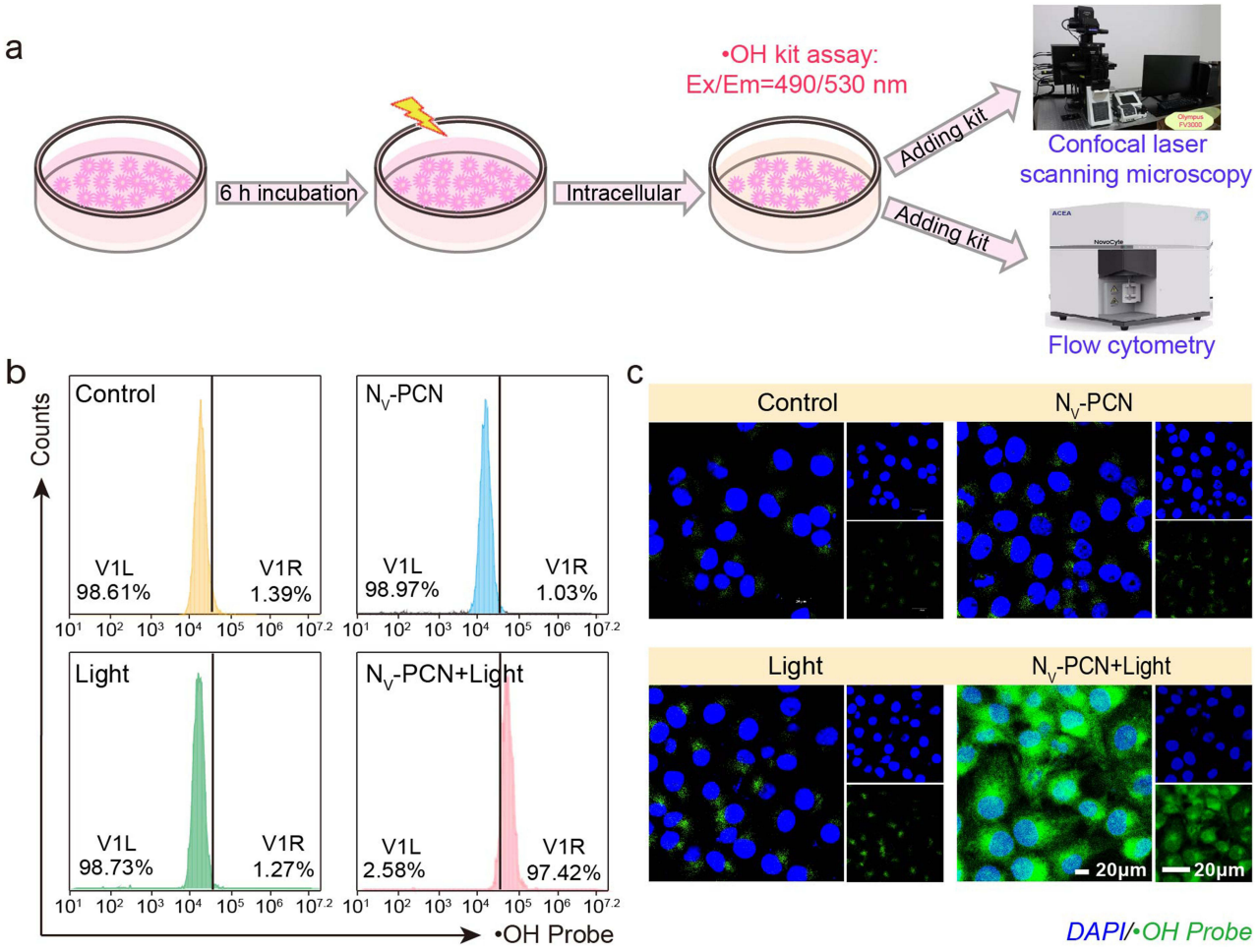

Figure 3 PDT definitely promoted tumoral •OH expression in vitro. (**a**)Depicts a schematic diagram of detecting intracellular •OH in Cal-27 cells that have been pre-exposed to light, utilizing a •OH fluorescent probe. (**b**) Flow-cytometry analysis of •OH production in Cal-27 cells. (**c**) CLSM images of Cal-27 cells exposed to various conditions, where green fluorescence reflects •OH expression.

increased in the N_V-PCN + light group, indicating that more •OH was generated. In Figure 3c, we can clearly see that the N_V-PCN + light group exhibits stronger green fluorescence intensity, indicating N_V-PCN possesses similar photocatalytic activity in biological applications. In that case, we propose that N_V-PCN, a novel light photocatalyst, can act as a Fenton-like agent to augment efficient intracellular expression of •OH and induce cell apoptosis, thus achieving PDT.

In Vitro Anticancer Effects of N_V-PCN Irradiated with LED Light

Prior to assessing the therapeutic effects of N_V-PCN upon white LED-light illumination, it was necessary to use the standard CCK-8 assay to evaluate the cytotoxic effects, which is a very important issue in the medical application of nanomaterials. After incubation with PCN and N_V-PCN for 24 h, no obvious cytotoxicity was observed in Cal-27 cells, even at concentrations up to 1 $mg{\cdot}mL^{-1}$, indicating the negligible cytotoxicity of PCN and N_V-PCN (Figure 4a and b). By contrast, when exposed to white LED light, cell viability gradually declined with increasing concentrations of N_V-PCN, and the cell viability of the group incubated with 2 $mg{\cdot}mL^{-1}$ N_V-PCN was the lowest among all groups. Nevertheless, even under nonirradiated conditions, 2 $mg{\cdot}mL^{-1}$ N_V-PCN still affected cell viability. Therefore, we selected 1 $mg{\cdot}mL^{-1}$ as the optimal concentration for subsequent cell experiments. When adding isopropanol (scavenger of •OH)[27] into the system (N_V-PCN + light group), cell viability was significantly enhanced (Figure 5a), which showed that •OH played an key role in the N_V-PCN photocatalytic inactivation of cancer cells. In addition, the larger red fluorescence area in the live and dead images for the N_V-PCN + light group corroborates the results of the CCK-8 assay

https://doi.org/10.2147/IJN.S515726

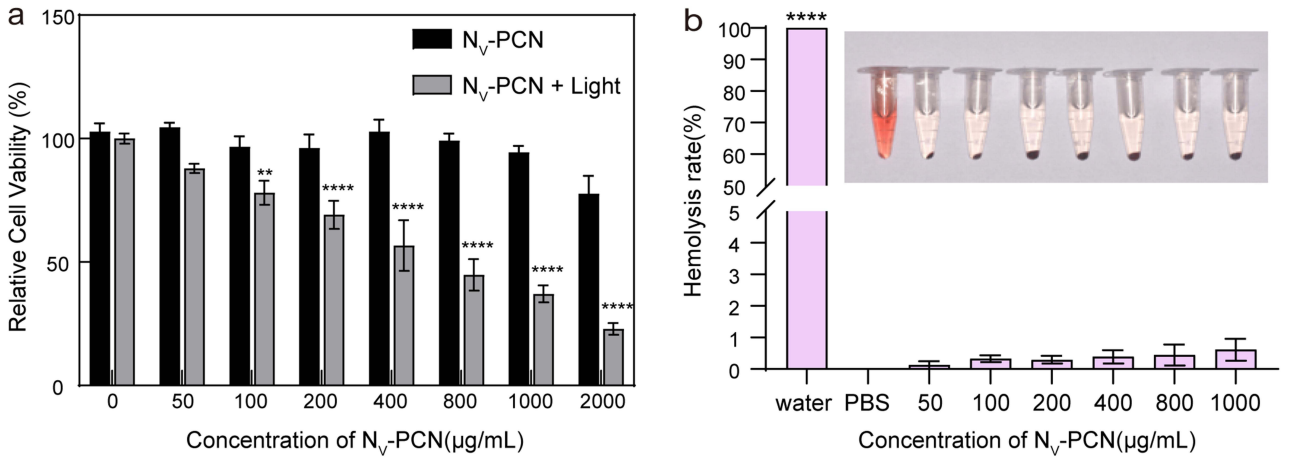

Figure 4 (**a**) Optimal concentrations of N_V-PCN acting on cells under light and dark conditions. **P<0.01, ****P<0.0001 compared to 0 μg/mL N_V-PCN + light. (**b**) Hemolysis values of various samples collected from the supernatants. ****P<0.0001 compared to the other groups.

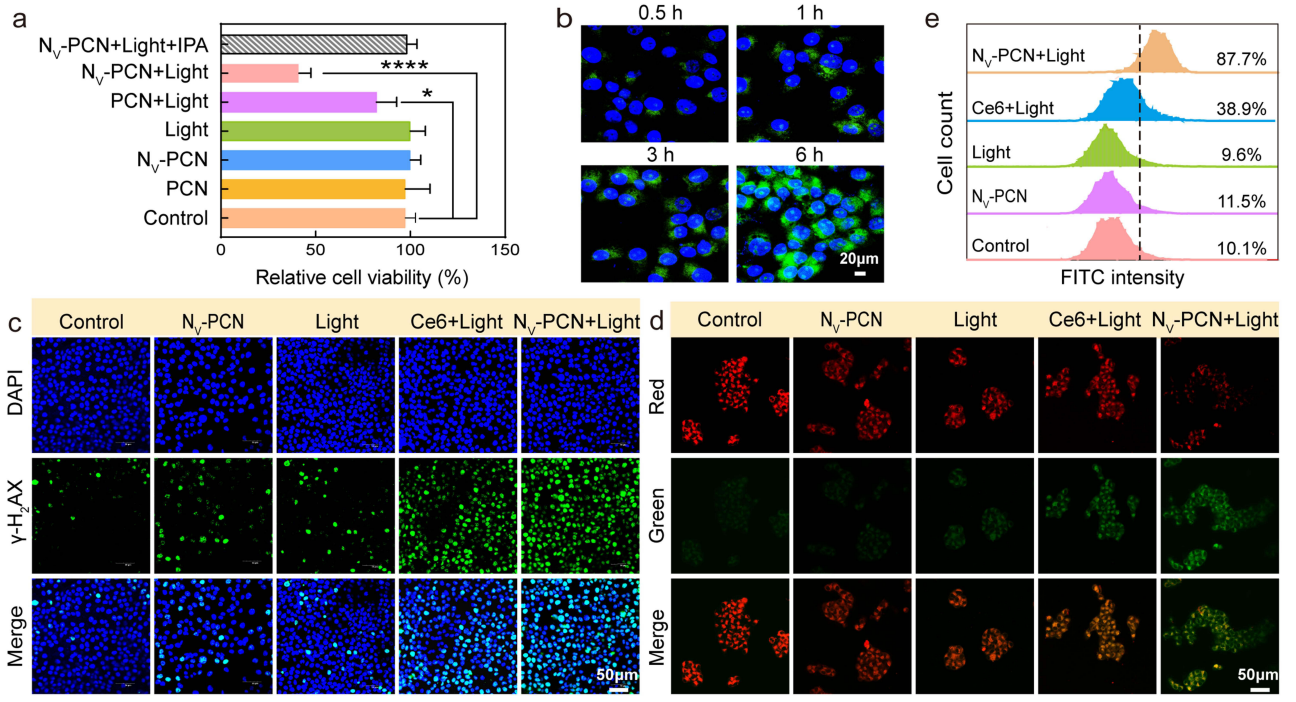

Figure 5 N_V-PCN as a photosensitizer induces dual damage to cancer nuclear DNA and mitochondria. (**a**) Relative viability of Cal-27 cells incubated with PCN and N_V-PCN at a concentration of 1 mg·cm^{-1} for 24 h with white LED light illumination for 30 min. (**b**) Cellular uptake evaluation of Cal-27 cells treated with N_V-PCN for 0.5–6 h using CLSM images. (**c**) Immunofluorescence images of γH_2AX foci (green) in Cal-27 cells treated withcontrol, N_V-PCN, light, Ce6 + light, and N_V-PCN + light. Cell nuclei were stained with DAPI (blue). (**d**) Confocal microscopy images of the JC-1 probe in Cal-27 cells. (**e**) Flow cytometry of total ROS generation in Cal-27 cells under different treatments using DCFH-DA as intracellular total ROS indicator. Significance calculated by one-way ANOVA: *P<0.05, ****P<0.0001 compared to the control group.

(Figure S6). The results suggest that N_V-PCN not only possesses great biocompatibility but also exhibits more efficient photodynamic killing ability of cancer cells than PCN under illumination. Therefore, this study deeply investigated the biological properties of N_V-PCN.

Next, assessment of the capacity of internalizing sufficient N_V-PCN in cancer cells was conducted, because this is critical for further therapeutic effects. Dark-field scattering microscopy was used to visualize the intracellular distribution of N_V-PCN. There was obvious signal enhancement in the N_V-PCN group compared with the control group, showing the efficient uptake of N_V-PCN by Cal-27 cells (Figure S7). As shown in Figure 5b, green fluorescence derived from N_V-

PCN is mainly concentrated in the cytoplasm and nucleus and intensifies with prolonged incubation time, indicating that the effective cellular uptake of N_V-PCN is dependent on incubation duration.

N_V-PCN, a potent photosensitizer, converts intracellular H_2O_2 to •OH under white LED-light irradiation. Among ROS, •OH exerts greater damage to cancer cells due to its more aggressive effect on nuclei, inducing DNA double-strand breaks.[28] Here, we evaluated DNA double-strand breaks by γH_2AX staining using immunofluorescence labeling (green) and Western blot. The results showed that a prominently higher density of γH_2AX foci occurred in the N_V-PCN + light and Ce6 + light group than in the control, light, and N_V-PCN-alone groups (Figure 5c and S8), indicating that N_V-PCN and Ce6 can greatly increase light-induced DNA damage. However, it has been observed that the occurrence of DNA damage in cancer cells promotes the initiation of DNA damage–repair mechanisms, which results in tumor resistance.[29]

Moreover, •OH has the potential to induce mitochondrial damage due to the superior reactivity of •OH.[30] Considering this, the mitochondrial functions of the different groups were evaluated by analyzing the MMP of cells. As depicted in Figure 5d, when compared with the single-treatment groups (control, N_V-PCN, and light), Cal-27 cells treated with Ce6 and N_V-PCN irradiated with light transformed more JC-1 polymer to JC-1 monomer on the mitochondria, suggesting declining MMP in Cal-27 cells, especially in the N_V-PCN + light group, revealing that more •OH produced by N_V-PCN during PDT eventuates in mitochondrial dysfunction. Ce6, an FDA-approved type II photosensitizer, predominantly functions by leveraging the available oxygen in tumors to generate singlet oxygen, a key mechanism behind its therapeutic effectiveness. Nonetheless, the tumor microenvironment is inherently hypoxic, implying that it lacks the sufficient substrate necessary for the generation of reactive oxygen species (ROS) that are crucial for inflicting mitochondrial damage.[31] Mitochondria regulate ROS and maintain cellular redox balance. Dysfunction in mitochondria boosts ROS, aggravating DNA damage and possibly leading to cellular dysfunction and disease progression.[32] To further verify the total intracellular ROS generation of N_V-PCN under LED illumination, DCFH-DA was used as a fluorescent probe to monitor the intracellular production of ROS. DCFH-DA is hydrolyzed by esterase after entering the cell to form DCFH, which can react with ROS in cells and exhibit green fluorescence. Notably, intense green fluorescence was observed in the N_V-PCN + light (Figure S9). In contrast, negligible fluorescence was observed in the control, N_V-PCN, and light groups. We also quantitatively detected the generation levels of total intracellular ROS in Cal-27 cells using flow cytometry (Figure 5e), and obtained similar results to the aforementioned.

In eukaryotic cells, mitochondria are critical for regulating intracellular energy.[33] After mitochondrial damage, intracellular ATP content decreases.[34] As shown in Figure 6a, compared with the single-treatment groups, the ATP content of the N_V-PCN + light group was significantly reduced, leading to the downregulation of DNA-damage repair. However, the Ce6 + light group exhibited enhanced damage repair compared to the N_V-PCN + light group. 53BP1 and GADD45A, key factors in the DNA damage–repair process,[35,36] were further evaluated. N_V-PCN + light treatment markedly decreased the protein expression of 53BP1 and GADD45A (Figure 6b). Additionally, the downregulation of 53BP1 and GADD45A was further confirmed by Western blot analysis (Figure 6c), and cancer cells treated with N_V-PCN + light exhibited failed DNA-damage repair.

Then, we evaluated their therapeutic effects upon light irradiation by EDU assays. As illustrated in Figure S10, there was 80%, 76%, and 60% cell proliferation of Cal-27 cells after treatment by N_V-PCN alone, light alone, and Ce6 + light, respectively, while only 26% survived under N_V-PCN + light treatment (smaller red fluorescence area, Figure 6d). Similarly, the Transwell assays revealed less cell migration in the N_V-PCN + light group than in the other three groups (Figure 6e). These results, along with previous findings, raise the possibility that compared to Ce6, N_V-PCN would induce a more powerful anticancer effect due to enhancing ROS generation and inhibiting cancer-cell proliferation under light irradiation.[37]

In addition, flow cytometry was utilized to quantitatively detect cell apoptosis under various treatments by annexin V–FITC/propidium iodide double staining. As shown in Figure 7a, no obvious apoptosis (early apoptosis or late apoptosis) was detected in the control, N_V-PCN-, or light-alone groups. On the contrary, when the cells were treated with Ce6 and N_V-PCN under light irradiation, early-apoptosis cells and late-apoptosis cells increased to 3.55% and 3.66% and to 14.51% and 33.42%, respectively. The results of Western blot and immunofluorescence analysis further confirmed that the apoptosis-related protein cleaved caspase 3 was activated and its expression was significantly greater in the N_V-PCN+ light group than in the other groups (Figure 6c, 7b), indicating that N_V-PCN + light cotreatment induces

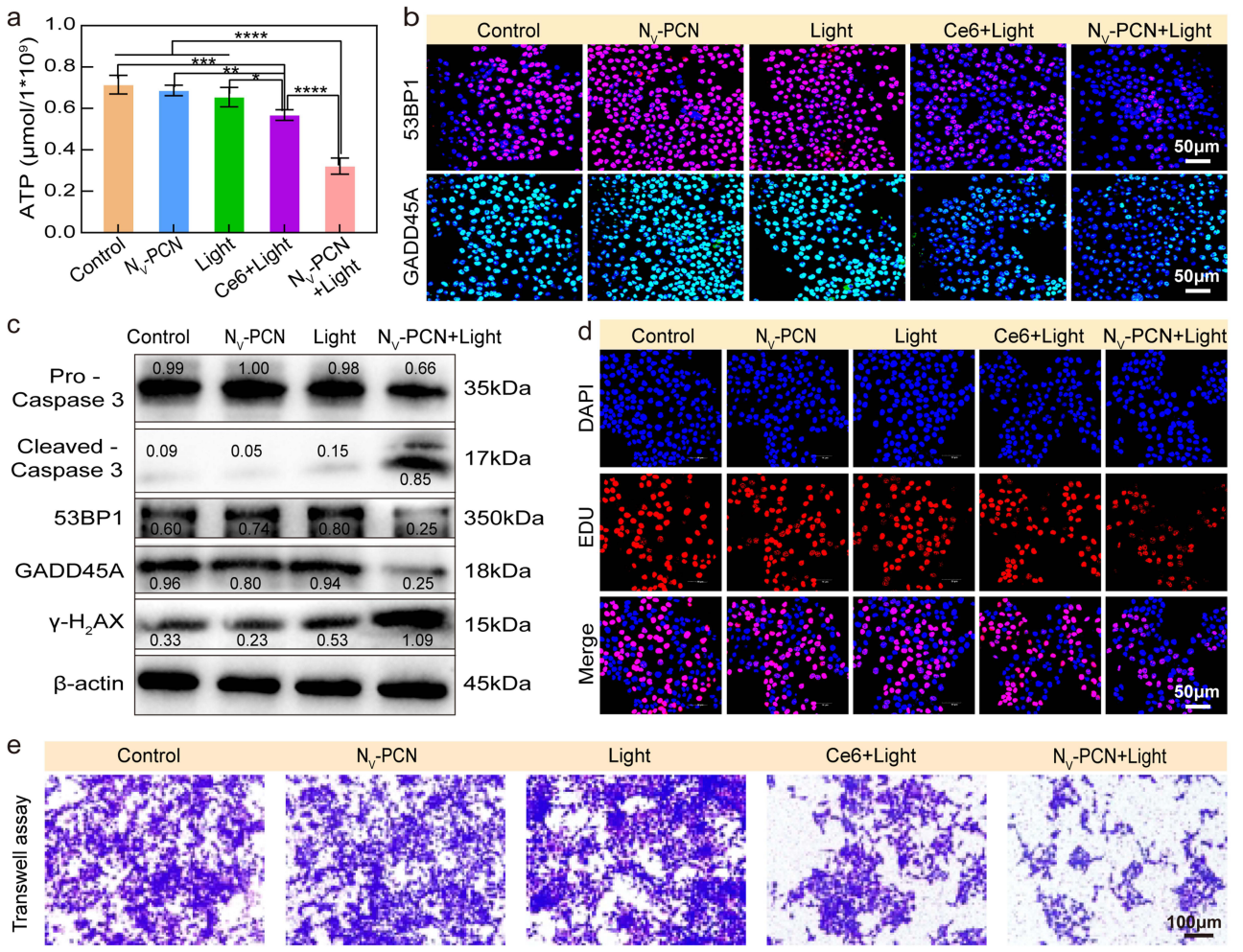

Figure 6 N_V-PCN-mediated PDT promoted Cal-27 cell apoptosis. (**a**) Intracellular ATP levels of Cal-27 cells after various treatments. (**b**) Expression of 53BP1 and GADD45A in Cal-27 cells examined by fluorescence microscopy. (**c**) Expression levels of γH2AX, GADD45A, 53BP1, pro-caspase 3, cleaved caspase 3, and β-actin proteins in cells treated for 24 h in different groups detected by Western blot experiments. β-actin protein was used as the internal control. (**d**) EDU assay of Cal-27 cells with control, N_V-PCN, light, Ce6 + light, and N_V-PCN + light. (**e**) Transwell assay of Cal-27 cells with control, N_V-PCN, light, Ce6 + light, and N_V-PCN + light. The concentration of N_V-PCN was 1 mg·mL^{-1}. Significance calculated by one-way ANOVA: **P*<0.05, ***P*<0.01, ****P*<0.001, *****P*<0.0001.

a powerful PDT effect and effectively triggers tumor-cell apoptosis. Taken together, these results indicate that the as-prepared N_V-PCN under LED irradiation enhanced anticancer activity by inducing •OH-mediated DNA damage and mitochondrial dysfunction, downregulating ATP, amplifying ROS storms, inhibiting DNA-damage repair, and upregulating apoptosis-related proteins.

In Vivo Antitumor Therapeutic Effect and Biosafety of N_V-PCN Irradiated with LED Light

The excellent performance of N_V-PCN at the cellular level prompted us to evaluate the PDT efficacy of N_V-PCN on solid cancers in BALB/c nude mice bearing Cal-27 tumors. Animal experiments were performed according to the protocols approved by the Ethics Committee of the Second Hospital of Shanxi Medical University (DW2023049). The treatment protocol is shown in Figure 8a. Prior to conducting the antitumor study, the biodistribution of Cy5.5–N_V-PCN after intratumoral injection was detected by tracking Cy5.5 fluorescence using an in vivo imaging system.[38] As shown in Figure 8b, the long-term distribution of Cy5.5–N_V-PCN fluorescence over 72 h indicates the excellent tumor-accumulation capacity of N_V-PCN.[39] It was observed that in addition to tumor tissue, kidney, one of the main metabolic organs, also

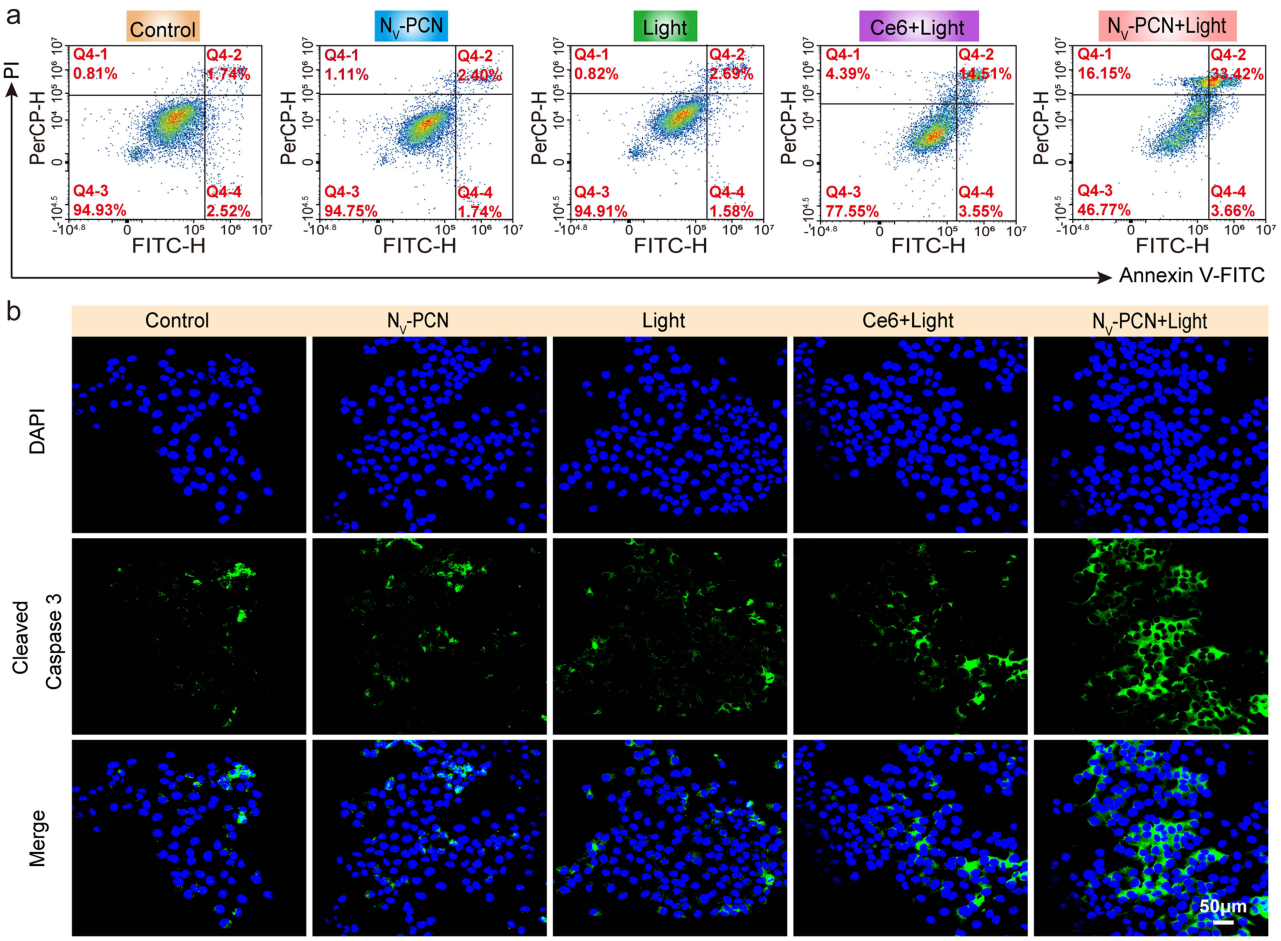

Figure 7 (**a**) Qualitative flow-cytometry data plot indicating the increase in apoptosis of Cal-27 cells after different treatments for 24 h. (**b**) Immunofluorescence images of cleaved caspase 3 (green) in Cal-27 cells treated with control, N_V-PCN, light, Ce6 + light, and N_V-PCN + light. Cell nuclei were stained with DAPI (blue).

exhibited much fluorescence aggregation compared with the control group within 6 h, indicating that some N_V-PCN can be excreted mainly through the kidneys without apparent impacts on the remaining organs.

Thereafter, the in vivo anticancer effects of N_V-PCN–mediated PDT were investigated. During the experiments, the weight of mice in all groups changed slightly within 22 days (Figure 8c), suggesting that N_V-PCN has no obvious systemic side effects in vivo. Compared with the control group and the single-treatment groups (N_V-PCN, light), Ce6 + light and N_V-PCN + light effectively suppressed tumor growth, with the N_V-PCN + light group showing a more pronounced effect (Figure 8d). The satisfactory photosensitizing effect is attributed to the enhanced generation of ROS, leading to the death of cancer cells in an apoptosis pathway. After 22 days, all mice were euthanized to harvest tumor tissue (Figure 8e) and weigh them to directly explore the efficacy of different treatments. The tumor weights are shown in Figure 8e. Mice that received Ce6 + light and N_V-PCN + light treatment had significantly smaller tumor volume, which matches well with the tumor-growth curves in Figure 8d, further indicating that N_V-PCN presents significant advantages in anticancer therapy.[40] The therapeutic effect was also confirmed by pathological results (Figure 8f). All groups showed varying degrees of tumor necrosis on H&E staining. Remarkably, the N_V-PCN + light group showed tumor-tissue damage (approximately 75% and 80%). Moreover, cancer cells in the N_V-PCN + light group exhibited the weakest Ki67 signal and the strongest TUNEL signal, showing that this treatment can maximally inhibit cell proliferation and promote cell apoptosis. It is particularly noteworthy that N_V-PCN PDT was confirmed to effectively increase the expression of γH_2AX and cleaved caspase 3, implying serious DNA damage and apoptosis.

Nanomedicine safety is a critical concern in its application in biomedicine. Consequently, experiments including H&E staining of main organs and blood hematology were performed to ensure the safe application of N_V-PCN and Ce6

https://doi.org/10.2147/IJN.S515726

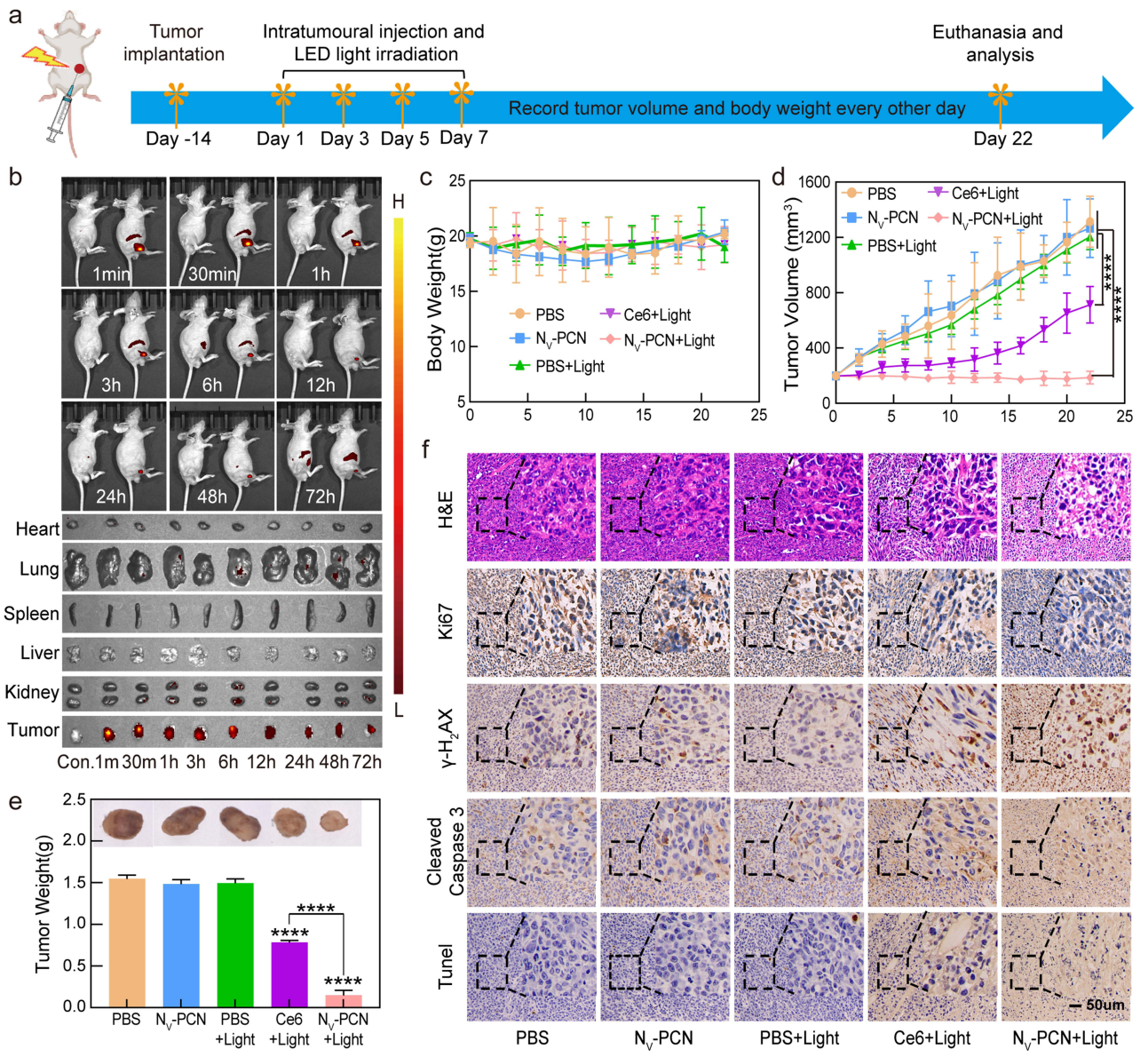

Figure 8 In vivo antitumor effect of N_V-PCN-mediated PDT. (**a**) Schematic of the therapeutic process for cancer-bearing nude mice. (**b**) Fluorescence images of Cal-27 cancer-bearing mice and ex vitro fluorescence images of major organs and tumor tissue after intratumoral injection of Cy5.5–N_V-PCN at different time points. (**c**) Time-dependent surveillance of body weight for mice with different treatments over 22 days (n=4). (**d**) Time-dependent surveillance of tumor volume for mice with different treatments over 22 days (n=4). (**e**) Cancer images of each group derived from BALB/c mice at day 22 posttreatment. (**f**) H&E and immunohistochemical staining of tumor tissue of mice after various treatments. Significance calculated by one-way ANOVA: ****P<0.0001.

in vivo. We collected the major organs (heart, liver, spleen, lung, and kidney) after different treatments for H&E staining, and the histological morphology of the major organs appeared unaffected in all the groups (Figure 9a). The blood biochemistry and hematology tests also showed negligible effects in the significant parameters (Figure 9b and c). All of these results demonstrate that N_V-PCN, similar to Ce6, is a safe nanoplatform for cancer therapy.

Methods

Catalyst Preparation

Pristine PCN was obtained by annealing melamine powder (10 g) at 550°C for 240 min (heating rate 3°C min^{-1}) and grinding it homogeneously under an air atmosphere. Subsequently, PCN (0.3 g) was subjected to annealing at 520°C for 60 min (heating rate of 10°C min^{-1}) under an argon atmosphere to synthesize N_V-PCN.

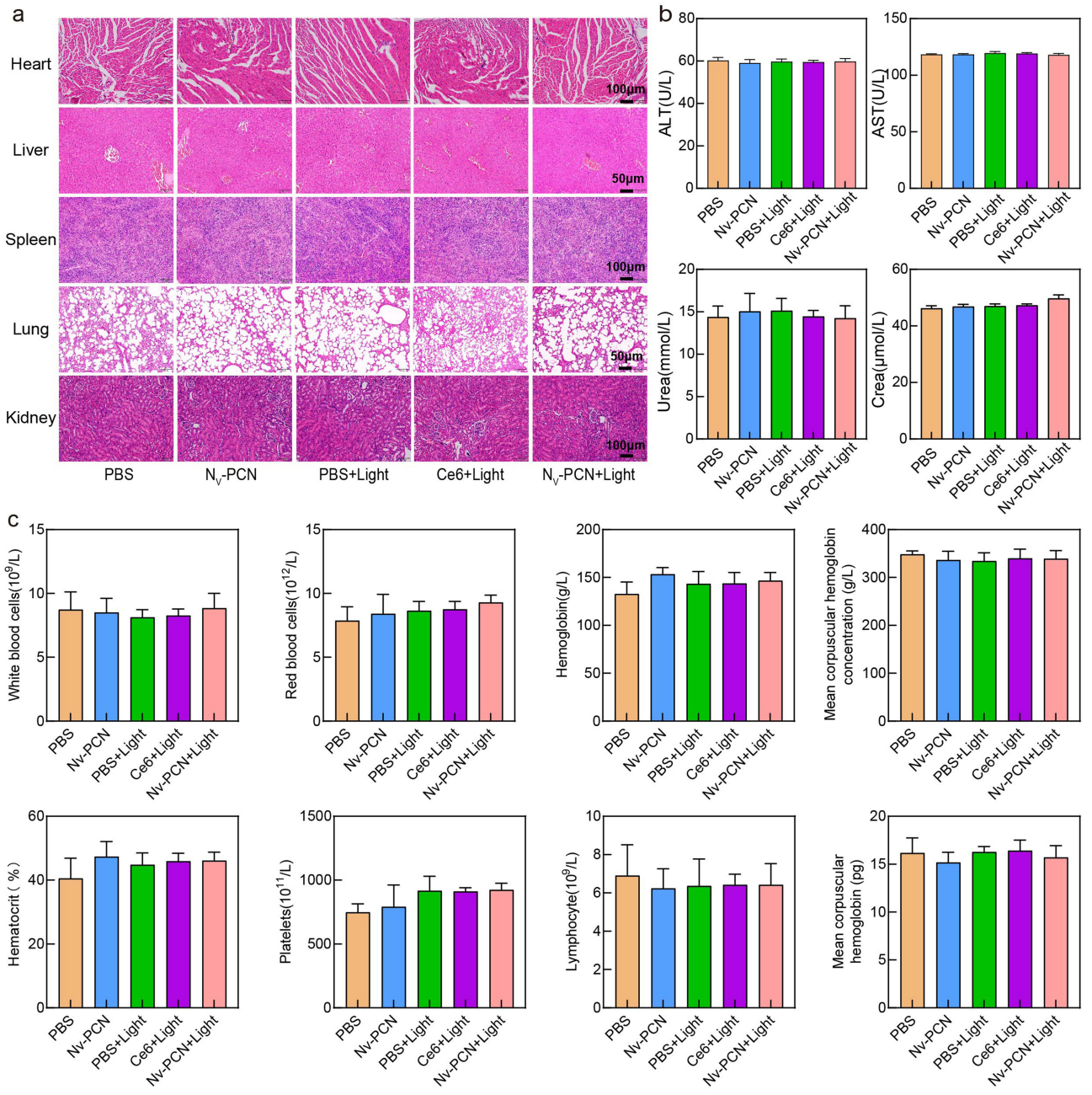

Figure 9 In vivo toxicity and safety assessment of N_V-PCN. (**a**) Hematoxylin and eosin–stained tissue sections from the mice to monitor histological changes in heart, liver, spleen, lung, and kidney 22 days after intratumoral injection of the N_V-PCN solution. (**b**) Blood biochemistry analysis of the mice treated with Ce6 and N_V-PCN. (**c**) Blood hematology analyses of mice on the last day.

Characterization

Transmission electron microscopy (TEM) images were obtained using a Tecnai G2 F20 STwin. Before measurement, a dispersion solution of PCN and N_V-PCN NSs was deposited on a carbon film supported by copper grids. X-ray diffraction (XRD) patterns were attained with a Bruker D8 Advance equipped with Cu Ka radiation (40 kV). Fourier-transform infrared (FTIR) spectra were recorded by a Bruker Tensor II spectrometer using a KBr pellet. X-ray photoelectron spectroscopy (XPS) was performed with a VG Scientific Escalab Mark II spectrometer. UV-vis diffuse reflectance spectra were obtained with a Shimadzu UV-3600 spectrometer. Electrochemical measurement was performed on a CHI 760E workstation using a conventional three-electrode configuration, where Ag/AgCl and platinum plates were used as reference and counter electrode, respectively. The working electrode was prepared by mixing catalyst (2.5 mg),

https://doi.org/10.2147/IJN.S515726

water (300 μL), ethanol (200 μL), and Nafion (5 wt%, 25 μL) evenly. The slurry (20 μL) was then spread to 0.5 cm^2 on a fluorine-doped tin oxide glass electrode. After the electrode had dried, the edge portion of the electrode was sealed with epoxy adhesive. Motto–Schottky plots and photocurrent signals were collected using 0.1 M of Na_2SO_4 solution as electrolyte. In situ DRIFT spectra were recorded in a sealed in-site reaction cell (equipped with Praying Mantis diffuse reflectance accessory and MCT detecor).

The catalyst was added to the reaction cell and processed at 100°C under argon for 1 h. Then, 10 μL of H_2O_2 solution was added, purged for 10 min under argon conditions, and the test data obtained after the catalyst had started to illuminate. In situ electron paramagnetic resonance (EPR) measurements were conducted on a Bruker EMXplus 10/12 spectrometer. For preparation of the test samples, 5 mg of catalyst was ultrasonically dispersed in 1 mL of acetonitrile, and 45 μL of the above mixture and 5 μL of H_2O_2 were mixed with 20 μL of DMPO acetonitrile solution (1 $mg \cdot \mu L^{-1}$). The EPR spectra were measured at an interval of 30 seconds and swept for 30 seconds with no superposition of signals. A BD FACSCanto II flow cytometer was used to perform flow-cytometry analyses. A multifunctional microplate reader was used to perform cell-viability and hemolysis experiments (Infinite M1000 Pro, Tecan). A white light–emitting diode (LED) with emission centered at 400–600 nm purchased from Shenzhen Zhongyu Technology (China) was used as the white-light source. The intensity of the white LED for photocatalysis and PDT was 50 $mW \cdot cm^{-2}$ for 30 min.

Cell Culture

Human oral squamous carcinoma cells (Cal-27) were obtained from the Chinese Academy of Sciences Cell Bank (Shanghai, China). Cal-27 cells were kept in DMEM (Gibco) supplemented with 10% FBS, 1% penicillin–streptomycin and 1% L-glutamine (Meilunbio) at 37°C in a cell incubator (Thermo Scientific) containing 5% CO_2. For cell passage, cells were digested with 0.25% trypsin–EDTA (Gibco) and then resuspended in fresh culture medium.

Measurement of Endogenous •OH

After coculturing N_V-PCN or Ce6 and Cal-27 cells in a 24-well plate (1×10^5 cells/well) for 6 h, cells were exposed or received no exposure to LED irradiation (50 $mW \cdot cm^{-2}$, 30 min). The culture medium was removed and each well washed repeatedly with PBS. Subsequently, the cells were incubated with HKOH-1r (MCE, HY-D1159) in a cell incubator for 30 min. •OH level was detected and quantified using confocal laser scanning microscopy (CLSM, Olympus, FV3000) and flow cytometry (Agilent Corporation, NovoCyte).

Cellular Uptake

The Cal-27 cells were seeded in 24-well plates (1×10^5 cells/well) and cultured for 24 h. After incubation with N_V-PCN, Cal-27 cells were fixed with 4% paraformaldehyde (PFA, Leagene), stained with DAPI (Beyotime), and finally the uptake of Cal-27 cells was observed with CLSM.

Cytotoxicity Assay

Cell viability was assessed using Cell Counting Kit 8 (CCK-8). The Cal-27 cells were cultured in 96-well plates (1.2×10^4 cells/well). After 24 h of incubation, the cells were treated with N_V-PCN (1 $mg \cdot mL^{-1}$, 100 μL) for 6 h and then irradiated with the white LED (50 $mW \cdot cm^{-2}$, 30 min). After 24 h, 100 μL of fresh DMEM containing CCK-8 (10%) was added and the treatment continued at 37°C for 30 min. Absorbance was then measured at 450 nm using a full-wavelength enzymograph (SpecteaMax plus 384, USA) to assess cell viability.

A fluorescent live/dead cell assay was applied to visualize the cell viability of N_V-PCN combined with visible light irradiation in Cal-27 cells. Typically, the cells were treated using the same method as described above and then stained with a Live/Dead Cell Staining Kit (BestBio, China) in accordance with the manufacturer's instruction. Afterwards, live and dead cells, emitting green and red fluorescence, respectively, were observed using CLSM.

In addition, hemocompatibility assays were used to measure the cytotoxicity of N_V-PCN. Fresh blood was obtained from BALB/c mice, red blood cells acquired via centrifugation (3000 rpm, 15 min), and then these were mixed with N_V-PCN concentrations of 200, 400, 600, 800, and 1000 $ug \cdot mL^{-1}$. PBS and ddH_2O were set as the negative and positive

control group, respectively. After incubation for 4 h, the solution was centrifuged (3000 rpm, 15 min) and the absorbance spectra of the supernatant were measured at 540 nm.

DNA Damage by N_V-PCN

Cal-27 cells (1×10^5/well) were seeded into 24-well plates for 24 h and then incubated with N_V-PCN or Ce6 (1 mg·mL^{-1}, 500 μL) for 6 h. Next, those cells were exposed or received no exposure to LED irradiation. PFA (4%) and Triton X-100 (0.5%) were used to fix and permeate the cells, respectively. Then, the cells were treated with blocking buffer (1% BSA, 30 min) at room temperature and further incubated with anti-phospho-histone γH_2AX rabbit monoclonal antibody (UpingBio, YP-Ab-01510, dilution 1:1000) at 4°C overnight. Then, fluorescein isothiocyanate (FITC; Beyotime Biotechnology, dilution 1:800) was added and incubated at room temperature for 1 h after being washed with PBS three times to remove excess antibody. Cell nuclei were stained by DAPI for 5 min. Finally, fluorescence images were acquired with CLSM.

Mitochondrial Membrane Potential Analysis

Cal-27 cells were inoculated in 24-well plates (1×10^5 cells/well) for 24 h. The cells were then treated with control, N_V-PCN, and Ce6 in the dark for 6 h with or without LED irradiation. JC-1 dyeing solution (configured according to manufacturer's instructions) was then added and incubated at 37°C for 20 min. Finally, the cells were washed three times with JC-1 dye buffer and images taken by CLSM.

Total Intracellular ROS Generation

Cal-27 cells (2×10^6/well) were seeded into six-well plates. Five groups were set: (a) control, (b) N_V-PCN, (c) light only, (d) Ce6 + light, and (e) N_V-PCN + light. Then, cells in the corresponding groups were incubated with control, N_V-PCN, and Ce6 (1 mg·mL^{-1}, 500 μL). After 6 h, the 2,7-dichlorodihydrofluorescein diacetate (DCFH-DA; Meilunbio, MA0219) was added as a fluorescence probe and the mixture incubated in the dark for 30 min. Afterwards, groups (c), (d), and (e) were disposed of" modified to "Afterwards, groups (c), (d), and (e) were exposed to illumination. Finally, flow cytometry and fluorescence microscopy (Leica, Germany) were used to study the generation of intracellular ROS.

Detection of Intracellular ATP

The Cal-27 cells were cultured in 96-well plates (1.2×10^4 cells/well). After 24 h of incubation, the cells were treated with N_V-PCN and Ce6 (1 mg·mL^{-1}, 100 μL) for 6 h, followed by light irradiation, then after incubation for another 24 h, the cells were collected. In conjunction with an ATP chemiluminescence assay kit (Elabscience, E-BC-F002), the fluorescence value of each well was detected by a Varioskan multifunctional enzyme labeler (Thermo Scientific, Varioskan LuX).

Immunofluorescence Staining

The Cal-27 cells were seeded into 24-well plates (1×10^5 cells/well) for 24 h and then incubated with N_V-PCN and Ce6 (1 mg·mL^{-1}, 500 μL) for 6 h. Next, they were exposed or received no exposure to LED irradiation. PFA (%) and Triton X-100 (0.5% were used to fix and permeate the cells, respectively. Then, the cells were treated with blocking buffer (1% BSA, 30 min) at room temperature and further incubated with 53BP1 (Beyotime), GADD45A (Bioss), and cleaved caspase 3 (Uping Bio) primary antibody at 4°C overnight. Subsequently, Cy5-labeled or FITC-labeled (Beyotime Biotechnology, dilution 1:800) goat anti-rabbit IgG was added and incubated at room temperature for 1 h after being washed with PBS three times to remove excess antibody. Cell nuclei were stained with DAPI for 5 min. Finally, fluorescence images were acquired with CLSM.

In Vitro Anticancer Effect of N_V-PCN

The Cal-27 cells were seeded in 24-well plates (1×10^5 cells/well) for 24 h and treated with N_V-PCN or Ce6 for 6 h. To evaluate the PDT effect, the cells were exposed or received no exposure to LED irradiation. The cells were then analyzed

using 5-ethinyl-2'-deoxyuridine (EdU; KeyGen), Transwell assays, and annexin V–FITC/propidium iodide (KeyGen, Nanjing, China) in accordance with the manufacturer's guidelines.

Western Blotting Assay

The Cal-27 cells were seeded in a six-well plate (2×10^6 cells/well) and cultured for 24 h. Then, N_V-PCN (1 mg·mL^{-1}) was added to two groups (N_V-PCN and N_V-PCN + light) for 6 h. The cells of the light or N_V-PCN + light group were irradiated with white LED light (50 mW·cm^{-2}, 30 min). After 24 h of incubation, cells were collected and lysed by precooled RIPA buffer for 30 min. After centrifugation (12,000 rpm) for 20 min at 4°C, the supernatant was mixed with the loading buffer and protein concentrations of the four groups determined using a BCA protein assay kit (KeyGen, BioTECH). Proteins were then separated and transferred. The membranes were blocked at room temperature (protein-free rapid blocking solution, Boster) for 20 min. After that, the membranes were incubated with primary antibodies overnight at 4°C. These antibodies were pro-caspase 3 (UpingBio, YP-Ab-00345, dilution 1:1500), cleaved caspase 3 (UpingBio, YP-Ab-00003, dilution 1:1500), γH2AX (UpingBio, dilution 1:1000), GADD45A (Bioss, bs-1360R, dilution: 1:200), 53BP1 (Abcam, ab243868, dion:luti 1:1000), and β-actin (ABclonal, AC038, dilution 1:10,000). Then, the membranes were washed and incubated with HRP-conjugated secondary antibody (UpingBio, YP848537-H, dilution 1:10000) for 1 h. Finally, stained with the ECL detection kit (Meilunbio, MA0186), the protein bands were observed using Compass software (Bio-Rad chemidoc XRS+, Universal Hood II) and the appropriate protein gray values calculated.

Transwell Assay

The migration ability of Cal-27 cells was detected by a Transwell assay. Cal-27 cells were seeded in 6-well plates at a density of 2×10^6 cells per well. After 24 h, the cells were treated with N_V-PCN (1 mg·mL^{-1}, 100 μL) for 6 h and then irradiated with white LED light (50 mW·cm^{-2}, 30 min) for another 24 h. The upper chambers of Transwell plates (Corning Inc.; Corning, NY, USA) use 8.0 μm-pore filters. Cal-27 cells in different groups were collected and seeded on the upper chambers (1.0×10^5 cells per chamber) in 200 μL serum-free medium. In contrast, the lower chambers were filled with 600 μL of DMEM medium containing 20% (V/V) FBS to induce cell invasion. After 24 h, the non-invading cells on the upper side of the filters were removed, and the invading cells on the lower side were fixed with 4% (W/V) PBS-buffered PFA for 30 min and stained with 0.2% (W/V) crystal violet for 10 min. The stained cells were visualized and counted in three random fields using an inverted microscope.

In Vivo Biodistribution and Cancer Accumulation of N_V-PCN

In order to evaluate the in vivo biodistribution of N_V-PCN, the healthy mice were intratumorally injected with Cy5.5-labeled N_V-PCN (5 mg·mL^{-1}, 50 μL). At time points of 1 min, 30 min, 1 h, 3 h, 6 h, 12 h, 24 h, 48 h, and 72 h), the mice were euthanized to collect the main organs (heart, liver, spleen, lung, and kidney) and tumor tissue. Fluorescence was visualized with a small-animal live optical 3D imaging system (PerkinElmer, IVIS Spectrum). Based on in vivo imaging-system observations, mice were euthanized after injection of Cy5.5–N_V-PCN at different time points, and then the harvested cancer tissue and major organs were analyzed by ex vivo fluorescence imaging.

In Vivo Anticancer Effects of N_V-PCN

To construct a tumor-bearing BALB/c mouse model, harvested Cal-27 cells were suspended in a suitable amount of PBS. Cancer cells were injected into the proximal axilla of the right hind limbs of mice to construct an OSCC mouse model. The mice were then injected with 50 μL (2×10^7 cells) of the suspension into their right hind-limb axilla. When tumors had grown to 100 mm^3, the mice were divided into four groups————(a) PBS, (b) N_V-PCN, (c) light only, (d) Ce6 + light, and (e) N_V-PCN + light—that were treated with PBS, N_V-PCN, or Ce6 solution via intratumoral injection every 2 days for a total of four times with or without light irradiation. The tumor volume was measured with a vernier caliper and calculated as (length × width^2)/2 for 22 days. After euthanasia, the cancer tissue and main organs (heart, liver, spleen, lung, kidney) were weighed, fixed in 4% PFA solution, and tissue slices embedded in paraffin. For further evidence of

cancer apoptosis, tumor slices were stained with HE, Ki67 (Abcam, ab15580), Tunel (Beyotime), γH_2AX, and cleaved caspase 3 antibody, and immunofluorescence images were captured by CLSM.

In Vivo Safety Assessment

Blood samples were collected from each group. About 100 μL of the samples were treated with anticoagulant (potassium EDTA) for hematology analysis. The residual blood was precipitated at room temperature for 2 h, and the plasma was collected by centrifugation at 3500 *g* for 10 min to assess liver (AST, ALT) and kidney (CRE, urea) function indices. Additionally, main organs (heart, liver, spleen, lung, kidney) were stained with H&E to observe changes in tissue structure using light microscopy. All analyses were conducted at Wuhan Xavier Biotechnology.

Statistical Analysis

All data are presented as means ± standard deviation (SD) of at least three independent replicates for each experiment. Statistical analysis was performed using GraphPad Prism 9. Data were compared using Student's *t* test and one-way ANOVA. Statistical differences are indicated by asterisks in the figures: $*P<0.05$, $**P<0.01$, and $***P<0.001$.

Conclusion

In summary, we designed nitrogen vacancy (N_V)–modified PCN (N_V-PCN) for PDT of Cal-27 cell-induced OSCC that effectively induced Cal-27-cell apoptosis by triggering DNA damage and inhibiting DNA-damage repair. The introduction of N_V not only further improved the cell accessibility of PCN by increasing the content of $–NH_2$ but also provided reactive sites for H_2O_2 reduction and facilitated carrier separation, which are beneficial for large-scale production of •OH. Moreover, EPR and intracellular •OH assays revealed that N_V-PCN exhibited superior •OH-generation efficiency under visible-light irradiation. Therefore, N_V-PCN leads to the explosion of •OH around the nuclei and mitochondria of Cal-27 cells under illumination, which effectively kills Cal-27 cells via synchronously leading to nucleus DNA damage and mitochondrial dysfunction. Then, mitochondrial dysfunction triggers an ROS storm to intensify DNA damage. It also attenuates the ATP energy chain to inhibit DNA-damage repair. Compared to the O_2-dependent photosensitizer Ce6, N_V-PCN-based PDT has stronger antitumor efficacy in vitro and in vivo. Therefore, this kind of nanoparticle not only represents an efficient photosensitizer for enhanced PDT of cancer but also opens up new avenues for in-depth study on carbon nitride-based cancer PDT.

Ethics Approval and Consent to Participate

The animal experiments were conducted in accordance with the Regulations on the Management of Laboratory Animals of Shanxi Province and *Guidelines for the Care and Use of Laboratory Animals* following the approval of the Ethics Committee of the Second Hospital of Shanxi Medical University (DW2023049). Every effort was made to reduce the number of mice used and alleviate their suffering.

Acknowledgments

Thank you to all the researchers in our laboratory for providing theoretical and technical support during the research.

Author Contributions

All authors made a significant contribution to the work reported, whether in the conception, study design, execution, acquisition of data, analysis and interpretation, or in all these areas, took part in drafting, revising, or critically reviewing the article, gave final approval to the version to be published, have agreed on the journal to which the article has been submitted, and agree to be accountable for all aspects of the work.

Funding

This work was supported by the National Natural Science Foundation of China (82071155, 82271023, and 82301052), Basic Research Project of Shanxi Province (202203021223006 and 202403021212211), Graduate Education Innovation Project of Shanxi Province (2023SJ139), Basic Research Project of Shanxi Province (202303021212131 and 202303021212132), and Health Commission of Shanxi Province (2022XM14).

Disclosure

The authors declare no competing interests.

References

1. Qian M, Cheng Z, Luo G, et al. Molybdenum diphosphide nanorods with laser-potentiated peroxidase catalytic/mild-photothermal therapy of oral cancer. *Adv Sci Weinh Baden-Wurtt Ger*. 2022;9(1):2101527. doi:10.1002/advs.202101527
2. Yu L, Xu Z, Zhu G, et al. High-performance photodynamic therapy of tongue squamous cell carcinoma with multifunctional nano-verteporfin. *Int J Nanomed*. 2024;19:2611–2623. doi:10.2147/IJN.S452060
3. Awwad SW, Serrano-Benitez A, Thomas JC, Gupta V, Jackson SP. Revolutionizing DNA repair research and cancer therapy with CRISPR-cas screens. *Nat Rev Mol Cell Biol*. 2023;24(7):477–494. doi:10.1038/s41580-022-00571-x
4. Shi H, Carter OWL, Ponte F, et al. A photodynamic and photochemotherapeutic platinum-iridium charge-transfer conjugate for anticancer therapy. *Angew Chem Int Ed*. 2024;63(23):e202400476. doi:10.1002/anie.202400476
5. Chen Q, Han L, Wu J, et al. A precise and intelligent nanomedicine for salivary adenoid cystic carcinoma treatment by combining antivascular photodynamic therapy and neuroinhibitory chemotherapy. *Adv Funct Mater*. 2024;34(13):2312732. doi:10.1002/adfm.202312732
6. Lietke S, Schmutzer M, Schwartz C, et al. Interstitial photodynamic therapy using 5-ALA for malignant glioma recurrences. *Cancers*. 2021;13(8):1767. doi:10.3390/cancers13081767
7. Xu S, Zhu X, Zhang C, Huang W, Zhou Y, Yan D. Oxygen and Pt(II) self-generating conjugate for synergistic photo-chemo therapy of hypoxic tumor. *Nat Commun*. 2018;9(1):2053. doi:10.1038/s41467-018-04318-1
8. Qing L, Shenshen W, Bin L, et al. "All-in-One" MnO2@PtAuRu nanoreactor for self-replenishing and cascade catalytic therapy of cancer. *Small*. 2024. doi:10.1002/smll.202405321
9. Du J, Zhou M, Chen Q, et al. Disrupting intracellular iron homeostasis by engineered metal-organic framework for nanocatalytic tumor therapy in synergy with autophagy amplification-promoted ferroptosis. *Adv Funct Mater*. 2023;34(17). doi:10.1002/adfm.202215244
10. Li D, Liu P, Tan Y, et al. Type I photosensitizers based on aggregation-induced emission: a rising star in photodynamic therapy. *Biosensors*. 2022;12(9):9. doi:10.3390/bios12090722
11. Bundy K, Kelly R, Brown E, Delahunty C. pH shifts and precipitation associated with metal ions in tissue culture. *Biomaterials*. 1985;6(2):89–96. doi:10.1016/0142-9612(85)90069-9
12. Zheng Y, Zhang L, Li Y, et al. Triptycene incorporated carbon nitride based donor-acceptor conjugated polymers with superior visible-light photocatalytic activities. *J Colloid Interface Sci*. 2022;622:675–689. doi:10.1016/j.jcis.2022.04.138
13. Xia P, Cao S, Zhu B, et al. Designing a 0D/2D S-scheme heterojunction over polymeric carbon nitride for visible-light photocatalytic inactivation of bacteria. *Angew Chem Int Ed Engl*. 2020;59(13):5218–5225. doi:10.1002/anie.201916012
14. Wang Y, Godin R, Durrant JR, Tang J. Efficient hole trapping in carbon dot/oxygen-modified carbon nitride heterojunction photocatalysts for enhanced methanol production from CO(2) under neutral conditions. *Angew Chem Int Ed Engl*. 2021;60(38):20811–20816. doi:10.1002/anie.202105570
15. Zhao D, Dong C-L, Wang B, et al. Synergy of dopants and defects in graphitic carbon nitride with exceptionally modulated band structures for efficient photocatalytic oxygen evolution. *Adv Mater Deerfield Beach Fla*. 2019;31(43):e1903545. doi:10.1002/adma.201903545
16. Palmer M, Björklund H, Olson L, Hoffer B. Trophic effects of brain areas on the developing cerebral cortex: II. electrophysiology of intraocular grafts. *Brain Res*. 1983;282(2):141–148. doi:10.1016/0165-3806(83)90092-5
17. Wu C, Yu G, Yin Y, et al. Mesoporous polymeric cyanamide-triazole-heptazine photocatalysts for highly-efficient water splitting. *Small Weinh Bergstr Ger*. 2020;16(37):e2003162. doi:10.1002/smll.202003162
18. Zhang Y, Huang Z, Dong C, et al. Synergistic effect of nitrogen vacancy on ultrathin graphitic carbon nitride porous nanosheets for highly efficient photocatalytic H2 evolution. *Chem Eng J*. 2022;431:134101. doi:10.1016/j.cej.2021.134101
19. Antil B, Kumar L, Reddy K, Gopinath C, Deka S. Direct thermal polymerization approach to N-rich holey carbon nitride nanosheets and their promising photocatalytic H2 evolution and charge-storage activities. *ACS Sustain Chem Eng*. 2019;7(10):9428–9438. doi:10.1021/acssuschemeng.9b00626
20. Zhang G, Xu Y, Rauf M, et al. Breaking the limitation of elevated coulomb interaction in crystalline carbon nitride for visible and near-infrared light photoactivity. *Adv Sci Weinh Baden-Wurtt Ger*. 2022;9(21):e2201677. doi:10.1002/advs.202201677
21. Tang H, Xia Z, Chen R, Liu Q, Zhou T. Oxygen doped G-C(3) N(4) with nitrogen vacancy for enhanced photocatalytic hydrogen evolution. *Chem Asian J*. 2020;15(21):3456–3461. doi:10.1002/asia.202000912
22. Liu M, Liu J, Zeng Z, et al. Steric hindrance effect induced photopurification of styrene oxide over surface modified polymeric carbon nitride. *Sep Purif Technol*. 2022;300:121929. doi:10.1016/j.seppur.2022.121929
23. Zhang X, He C, Chen Y, et al. Cyclic reactions-mediated self-supply of H(2)O(2) and O(2) for cooperative chemodynamic/starvation cancer therapy. *Biomaterials*. 2021;275:120987. doi:10.1016/j.biomaterials.2021.120987
24. He Z, Guo Y, Chen J, et al. Unsaturated phospholipid modified FeOCl nanosheets for enhancing tumor ferroptosis. *J Mater Chem B*. 2023;11(9):1891–1903. doi:10.1039/d2tb01854c
25. Huang R, Ni N, Su Y, et al. Chargeable persistent luminescence 3d-printed scaffolds: a stepwise tactic for osteosarcoma treatment. *Chem Eng J*. 2024;479:147436. doi:10.1016/j.cej.2023.147436
26. Gao Y, Tong H, Li J, et al. Mitochondria-targeted nanomedicine for enhanced efficacy of cancer therapy. *Front Bioeng Biotechnol*. 2021;9:720508. doi:10.3389/fbioe.2021.720508
27. Xu W, Kang Y, Jiao L, et al. Tuning atomically dispersed fe sites in metal-organic frameworks boosts peroxidase-like activity for sensitive biosensing. *Nano-Micro Lett*. 2020;12(1):184. doi:10.1007/s40820-020-00520-3
28. Xu M, Qian Y, Li X, et al. Janus ACSP nanoparticle for synergistic chemodynamic therapy and radiosensitization. *ACS Appl Mater Interfaces*. 2024;16(14):17242–17252. doi:10.1021/acsami.4c00499
29. Wang Y, Gao B, Zhang L, et al. Meiotic protein SYCP2 confers resistance to DNA-damaging agents through R-loop-mediated DNA repair. *Nat Commun*. 2024;15(1):1568. doi:10.1038/s41467-024-45693-2

30. Ding X, Wang T, Bai S, et al. A dual heat shock protein down-regulation strategy using PDA/Cu/ICG/R controlled by nir "switch" enhances mild-photothermal therapy effect. *Adv Healthc Mater*. 2023;12(27):e2300929. doi:10.1002/adhm.202300929
31. Zhang Y, Jia R, Wang X, et al. Targeted delivery of catalase and photosensitizer Ce6 by a tumor-specific aptamer is effective against bladder cancer in vivo. *Mol Pharm*. 2024;21(4):1705–1718. doi:10.1021/acs.molpharmaceut.3c01047
32. Miyakawa Y, Otsuka M, Shibata C, et al. Gut bacteria-derived membrane vesicles induce colonic dysplasia by inducing DNA damage in colon epithelial cells. *Cell Mol Gastroenterol Hepatol*. 2024;17(5):745–767. doi:10.1016/j.jcmgh.2024.01.010
33. Feng X, Lin T, Chen D, et al. Mitochondria-associated ER stress evokes immunogenic cell death through the ROS-PERK-eIF2α pathway under PTT/CDT combined therapy. *Acta Biomater*. 2023;160:211–224. doi:10.1016/j.actbio.2023.02.011
34. Duan C, Wang Z, Wu J, et al. Fut2 deficiency promotes intestinal stem cell aging by damaging mitochondrial functions via down-regulating A1,2-fucosylation of Asah2 and Npc1. *Res Wash DC*. 2024;7:0343. doi:10.34133/research.0343
35. Zhao B, Ma Z, Ding S, et al. Catalytic MnWO4 nanorods for chemodynamic therapy synergized radiotherapy of triple negative breast cancer. *Adv Funct Mater*. 2023;33(47). doi:10.1002/adfm.202306328
36. You W, Liu S, Ji J, et al. Growth arrest and DNA damage-inducible alpha regulates muscle repair and fat infiltration through atp synthase F1 subunit alpha. *J Cachexia, Sarcopenia Muscle*. 2023;14(1):326–341. doi:10.1002/jcsm.13134
37. Guney Eskiler G, Deveci Ozkan A, Sozen Kucukkara E, Kamanlı AF, Gunoğlu B, Yıldız MZ. Optimization of 5-aminolevulinic acid-based photodynamic therapy protocol for breast cancer cells. *Photodiagnosis Photodyn Ther*. 2020;31:101854. doi:10.1016/j.pdpdt.2020.101854
38. Guo H, Liu L, Hu Q, Dou H. Monodisperse ZIF-8@dextran nanoparticles co-loaded with hydrophilic and hydrophobic functional cargos for combined near-infrared fluorescence imaging and photothermal therapy. *Acta Biomater*. 2022;137:290–304. doi:10.1016/j.actbio.2021.10.006
39. Chang R, Wang P-Y, Tseng C-L. New combination/application of polymer-based nanoparticles for biomedical engineering. *Adv Exp Med Biol*. 2018;1078:271–290. doi:10.1007/978-981-13-0950-2_14
40. Bhanja D, Wilding H, Baroz A, et al. Photodynamic therapy for glioblastoma: illuminating the path toward clinical applicability. *Cancers*. 2023;15(13):13. doi:10.3390/cancers15133427

International Journal of Nanomedicine

Dovepress
Taylor & Francis Group

Publish your work in this journal

The International Journal of Nanomedicine is an international, peer-reviewed journal focusing on the application of nanotechnology in diagnostics, therapeutics, and drug delivery systems throughout the biomedical field. This journal is indexed on PubMed Central, MedLine, CAS, SciSearch®, Current Contents®/Clinical Medicine, Journal Citation Reports/Science Edition, EMBase, Scopus and the Elsevier Bibliographic databases. The manuscript management system is completely online and includes a very quick and fair peer-review system, which is all easy to use. Visit http://www.dovepress.com/testimonials.php to read real quotes from published authors.

Submit your manuscript here: https://www.dovepress.com/international-journal-of-nanomedicine-journal